
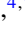



Magneto-optical conductivity and giant Faraday-Kerr rotation in Floquet topological insulatorsMuzamil Shah ¹, Muhammad Qasim Mehmood ^{2,*}, Yee Sin Ang ³, Muhammad Zubair ^{4,†} and Yehia Massoud ^{4,‡}¹*Department of Physics, Zhejiang Normal University, Jinhua 321004, China*²*Department of Electrical Engineering, MicroNano Laboratory, Information Technology University of the Punjab, Lahore 56000, Pakistan*³*Science, Mathematics and Technology (SMT) Cluster, Singapore University of Technology and Design (SUTD), Singapore 487372*⁴*Innovative Technologies Laboratories (ITL), King Abdullah University of Science and Technology (KAUST), 23955-6900, Saudi Arabia*

(Received 16 November 2022; revised 9 April 2023; accepted 11 May 2023; published 7 June 2023)

We study the surface state-dependent magneto-optical properties of an ultrathin Floquet topological insulator (FTI) under the influence of an external perpendicular magnetic field in the terahertz frequency regime. Under the Floquet picture, we treat the circularly polarized off-resonant light as an external perturbation that introduces a mass gap at the Dirac cone, thus, making the surface state Dirac fermions massive. By tuning the optical field energy in the FTI thin-film system, various electronic phase transitions can be driven between the trivial insulator state and the band insulator state. Using Kubo formalism, we derive the real and imaginary parts of the longitudinal and Hall conductivities and demonstrate that these conductivities are sensitively influenced by the strength of the off-resonant optical field, magnetic field, and chemical potentials. On the other hand, topological insulators exhibit strong magneto-optic effects. We further compute the Kerr and Faraday rotation angles and show that giant Kerr and Faraday rotations can be achieved in a FTI thin film by external tuning knobs, such as magnetic and off-resonant optical fields. The Kerr and Faraday rotations in symmetric (top) and antisymmetric (bottom) topological surface states can be controlled for interband and intraband transitions via gate bias voltage. Our results reveal the FTI as an intriguing versatile system whose magneto-optical properties can be effectively tuned optically, magnetically and electrically, thus, uncovering the strong photonics and optoelectronics device application potentials of the FTI.

DOI: [10.1103/PhysRevB.107.235115](https://doi.org/10.1103/PhysRevB.107.235115)**I. INTRODUCTION**

Over the past 15 yr, the field of topological materials has evolved rapidly and has attracted huge interest due to their tremendous importance in fundamental physics as well as device applications [1–4]. Topological insulators (TIs) represent an important member of the topological material family in which the bulk is electrically insulating, but the surface is electrical conductive with gapless surface states (SSs). The SSs typically carry helical quasiparticles as described by the two-dimensional massless Dirac-type Hamiltonian, such as the quasiparticles residing at the K and K' points of graphene [5] and are robust against smooth local deformations and backscattering by time-reversal symmetry (TRS) [6]. By breaking the TRS in TIs, exotic quantum phenomena occur including the quantum anomalous Hall effect [7–9], topological magnetoelectric effect [10–12], and the formation of magnetic monopoles [13]. Culcer group has pointed out the intrinsic

origin of the anomalous planar Hall effect in two-dimensional (2D) heavy-hole gas in the presence of in-plane magnetic field B_{\parallel} [14]. Recently, second-order responses, such as the linear photocurrents, injection currents, the nonlinear Hall effect, quantized circular photogalvanic effect, and quantized circular photocurrents in quantum systems have attracted huge interest [15–23].

One of the significant challenges in the transport properties of the topological insulators has been the difficulty in separating bulk contributions from the surface state contribution. Thin-film topological insulator material provides an ideal system when compared to semi-infinite TI slabs in this respect as the bulk contribution to transport is significantly reduced. A TI ultrathin film has both top and bottom surfaces, each of which can host SS Dirac electrons. The symmetric and antisymmetric surfaces of the TI thin film are coupled to each other due to the finite thickness d of the film. The overlapping of the symmetric and antisymmetric SSs wave functions results in quantum tunneling between SSs and opens an energy gap Δ_H emerges at the Dirac points [24,25]. The band gap at the top and bottom SSs can be controlled by tuning the thickness of the thin film.

The experimental realization of the electronic phases and quantum phase transitions (QPTs) in 2D materials, such as graphene, Dirac-Weyl semimetals, silicene, and transition-metal dichalcogenides, triggered a great interest in the scientific community to discover new quantum phases of matter. QPT can be extrinsically induced in TIs through different external stimuli, such as an external electric and magnetic

*qasim.mehmood@itu.edu.pk

†muhammad.zubair.3@kaust.edu.sa

‡yehia.massoud@kaust.edu.sa

field [26,27]. An external time-periodic perturbation driving on a TI system generates helical edge states and is known as Floquet topological insulators (FTIs) [28]. Recently, the SSs of TIs driven by off-resonant circularly polarized optical fields have become a subject of immense interest [29,30]. By varying the optical field strength, the FTI thin film is predicted to transition from a quantum pseudo-spin Hall insulator (QP-SHI) phase to a photoinduced quantum Hall (P-QH) phase. Under the application of a perpendicular external magnetic field B , the quantization of the energy eigenstates exhibits discrete Landau levels (LLs) in two materials. The characteristics of the Dirac electrons in graphene under an external magnetic-field B have been studied theoretically and experimentally investigated [31–34]. In 2D electron gas (2DEG), the Landau levels are equally spaced but in graphene due to its unusual electronic energy dispersion, the Landau levels are nonequally spaced. The energy dispersion of graphene is proportional to \sqrt{nB} , where n denotes Landau levels, and B is the magnetic field. The conduction and valence bands in graphene are mirror-symmetric with $E = 0$ axis, whereas the $n = 0$ LLs are residing at zero energy [31]. Optical transitions between these discrete Landau levels produce absorption peaks in the magneto-optical conductivity (MO) spectra. Magneto-optical properties of 2D materials, for example, graphene [31], silicene [35,36], MoS₂ [37], and phosphorene [38] have been studied in detail.

In recent years, the light-induced quantum effects in graphene and other two-dimensional quantum materials have generated a strong interest in the condensed-matter physics community [28,39,40]. It has been theoretically demonstrated that the strong interaction between massless Dirac fermions in graphene and circularly polarized photons results in metal-to-insulator transition [41,42]. It has been also shown that a strong interaction of a 2DEG with a dressing electromagnetic field drastically changes its transport properties [43,44]. In this context, it is worthwhile to mention that the Floquet theory of various Dirac materials with linear electron dispersion has been well studied. However, the systematical study of magneto-optical responses and the optoelectronic responses of the FTI thin film remains limited, thus, far. As the FTI can be sensitively modulated by various external stimuli, such as electrical, magnetic, and optical fields, a systematic study of its magneto-optical responses may, thus, serve as a versatile tool to probe the physical properties of the FTI and reveal its strong potential for application in photonics and optoelectronics.

In this article, we study the surface state-dependent magneto-optical conductivity of the FTI thin film under the influence of perpendicular magnetic and circularly polarized optical fields using Kubo formalism. The energy dispersions of the FTI thin film with and without a magnetic field are discussed under distinct topological phases. We investigate the real and imaginary components of the magneto-optical conductivity in the presence of a quantized magnetic field for both symmetric and antisymmetric surface states. We study the possible optical transitions in the FTI thin film that occur between different Landau levels by absorption of right-/left-handed circularly polarized photons subjected to optical selection rules. We further calculate the magneto-optical absorption spectra versus photon energy for distinct

topological phases whereas keeping the magnetic field and chemical potential fixed. We also explore the effects of doping of the LLs on the magneto-optical absorption spectra by changing the electron concentration. We also study the Kerr and Faraday rotations in the FTI thin film. The Kerr/Faraday rotations are nonreciprocal phenomena that occur in an active and transparent medium in which the polarization of the reflected/transmitted linearly polarized plane wave is rotated in a magnetic-field B . The present study of the magneto-optical effects details the impact of an external magnetic field, off-resonant optical field, electron concentration, incident photon energy, and incident angle.

The magnitude of Faraday rotation angle in graphene is about 6° in a magnetic field of strength 7 T at low frequencies [45]. In contrast to graphene, the amount of the maximum Faraday and Kerr rotation angles in the FTI thin film exceeds $\approx 4.4^\circ$ and $\approx 15^\circ$ for $B = 5$ T respectively. The surface state-dependent magneto-optical effects of the FTI thin film systems may open avenues for to design of novel photonic, optoelectronics, and optospinronic devices. In addition, the Kerr and Faraday rotations are important and suitable experimental tools for probing distinct topological phases of topological materials and can be used for practical applications, such as Faraday rotators, magnetic-field sensing, current sensors, isolators, optical modulation, and communication.

This article is organized in the following way. We discuss the basic Hamiltonian of the FTI ultrathin film subjected to circularly polarized optical and magnetic fields and calculate the eigenenergies and eigenstates of the quantum system with and without a magnetic field in distinct topological phases in Sec. II A. In Secs. II B and III A, we derive the real and imaginary components for the longitudinal and transverse Hall MO of the FTI thin film and provide numerical results for different values of magnetic and optical fields. In Sec. III B, we discuss the effect of the chemical potential modulation on the magneto-optical conductivity of the FTI thin films. Section III C includes a discussion on the Kerr and Faraday rotations for different magnetic, optical fields, and chemical potentials. We conclude our results in Sec. IV.

II. FORMALISM

A. System Hamiltonian

The 2D Dirac-like Hamiltonian of the SSs of the FTI thin films subjected to a circularly polarized optical field is as follows [46–48]:

$$H_{\tau_z}^\eta = \hbar v_F (k_y \sigma_x - k_x \sigma_y) + \Delta_{\tau_z}^\eta \sigma_z, \quad (1)$$

where $v_F = 5 \times 10^5$ m/s being the Fermi velocity [12], σ_x , σ_y , and σ_z are the Pauli matrices, $\Delta_{\tau_z}^\eta = \tau_z \Delta_H + \eta \Lambda_\omega$ is the Dirac mass, $\tau_z = \pm 1$ is for top/bottom (symmetric/antisymmetric) SSs, and $\eta = \pm 1$ represents the right/left circular polarization off-resonant light. Δ_H is the hybridization potential between the symmetric and the antisymmetric SSs, which depends on the thickness [24,25]. Λ_ω represents the mass term induced by the off-resonant circularly polarized optical field. It must be noted that the Λ_ω breaks the TRS. The dispersion relation of the FTI thin film corresponding to Eq. (1)

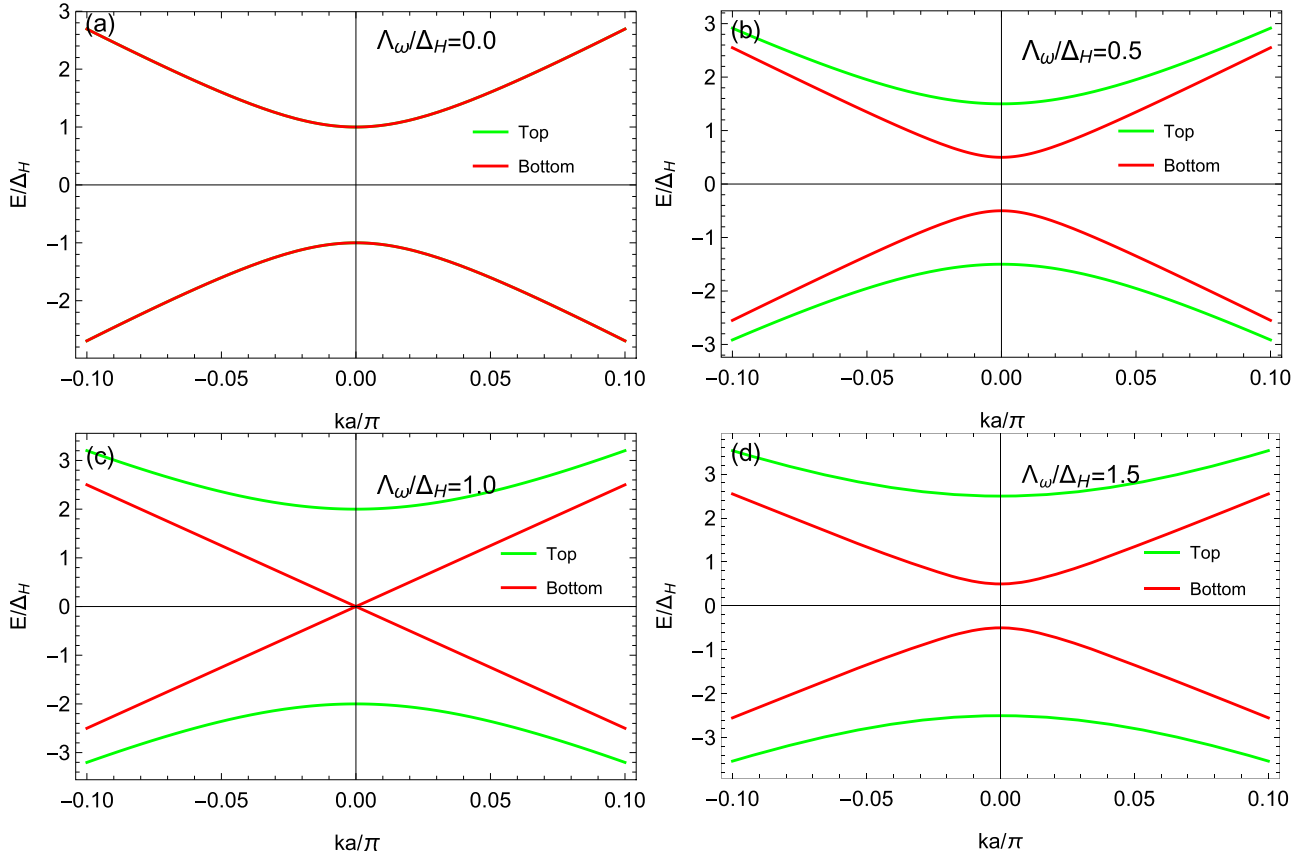


FIG. 1. Energy dispersion $\mathcal{E}_{\tau_z}^{\eta,\lambda}$ of the Floquet topological thin film in distinct topological phases for right-handed circularly polarized (RHCP) irradiated light. (a) $\Lambda_\omega = 0$, (b) $\Lambda_\omega = 0.5\Delta_H$, (c) $\Lambda_\omega = \Delta_H$, and (d) $\Lambda_\omega = 1.5\Delta_H$. The top and bottom SS bands are represented by solid green and red curves, respectively. We set $v_F = 5 \times 10^5$ m/s and $\Delta_H = 4$ meV [46].

can be obtained as

$$\mathcal{E}_{\tau_z}^{\eta,\lambda} = \lambda \sqrt{\hbar^2 v_F^2 k^2 + (\Delta_{\tau_z}^\eta)^2}, \quad (2)$$

where $\lambda = \pm 1$ denotes the conduction/valance bands. The normalized wave function of the system is given by

$$\psi_{\tau_z}^\eta(\mathbf{k}) = \begin{pmatrix} \psi_A \\ \psi_B \end{pmatrix} = \frac{1}{\sqrt{2A}} \begin{pmatrix} \sqrt{1 + \lambda \cos \theta} \\ \lambda \sqrt{1 - \lambda \cos \theta} e^{i\tau_z \phi_k} \end{pmatrix} e^{i\mathbf{k}\cdot\mathbf{r}}, \quad (3)$$

where $A = L_x L_y$ denotes the area of the FTI thin-film sample, $k = \sqrt{k_x^2 + k_y^2}$, $\cos \theta = \Delta_{\tau_z}^\eta / \mathcal{E}_{\tau_z}^{\eta,\lambda}$, and $\sin \theta = \hbar v_F k / \mathcal{E}_{\tau_z}^{\eta,\lambda}$. The electronic spectra of FTI are shown in Figs. 1(a)–1(d) for the RHCP irradiated light where solid green curves correspond to the top SSs and solid red curves represent the bottom SSs bands. First, we consider that the irradiated off-resonant optical field $\Lambda_\omega = 0$. We can observe that the spectrum remains gapped with no spin splitting in the surface bands as depicted in Fig. 1(a). For a finite optical field ($\Lambda_\omega < \Delta_H$), the pseudospin degeneracy is lifted, the top (bottom) SSs energy bands move upward (downward), and the quantum system stays as a QPSH phase as illustrated in Fig. 1(b). As applied circularly polarized laser intensity is increased, the band gap between the top SSs decreases and at the charge neutrality point (CNP) the Dirac cone closes completely as presented in Fig. 1(c). For $\Lambda_\omega > \Delta_H$, all gaps are opened, and this opening and closing of the band gap signify a QPT from a QPSHI phase to a P-QH phase as shown in Fig. 1(d). For the

left-handed circularly polarized (LHCP) irradiated optical field, the Floquet topological thin film stays the same as the RHCP except the bands related to the symmetric (antisymmetric) SSs move downward (upward).

We now consider the SS Hamiltonian of the FTI thin film by including an external perpendicular magnetic-field B . Working in the Landau gauge and employing the Peierls substitution with vector potential $(0, Bx, 0)$, our Hamiltonian becomes

$$H_{\tau_z\eta} = \hbar v_F [(k_y - eBx/\hbar)\sigma_x - k_x\sigma_y] + \Delta_{\tau_z\eta}\sigma_z, \quad (4)$$

Diagonalizing the above Hamiltonian given in Eq. (4) yields the low-energy Landau-level dispersion,

$$\mathcal{E}_{n,\tau_z}^{\eta,\lambda} = \lambda \sqrt{E_B^2 |n| + (\Delta_{\tau_z}^\eta)^2}, \quad (5)$$

$$\mathcal{E}_{0,\tau_z}^{\eta,\lambda} = -\Delta_{\tau_z}^\eta, \quad (6)$$

where $\lambda = \pm 1$ represents the conduction/valance bands and $E_B = v_F \sqrt{2eB\hbar}$. The corresponding solutions of the normalized eigenstates are as follows:

$$\Phi_{n,\tau_z}^{\eta,\lambda} = \frac{e^{ik_y y}}{\sqrt{L_y}} \begin{pmatrix} -i\mathcal{A}_{n,\tau_z}^{\eta,\lambda} |n-1\rangle \\ \mathcal{B}_{n,\tau_z}^{\eta,\lambda} |n\rangle \end{pmatrix}. \quad (7)$$

For $n = 0$, Landau levels,

$$\Phi_{0,\tau_z}^{\eta,\lambda} = \frac{e^{ik_y y}}{\sqrt{L_y}} \begin{pmatrix} 0 \\ |0\rangle \end{pmatrix}, \quad (8)$$

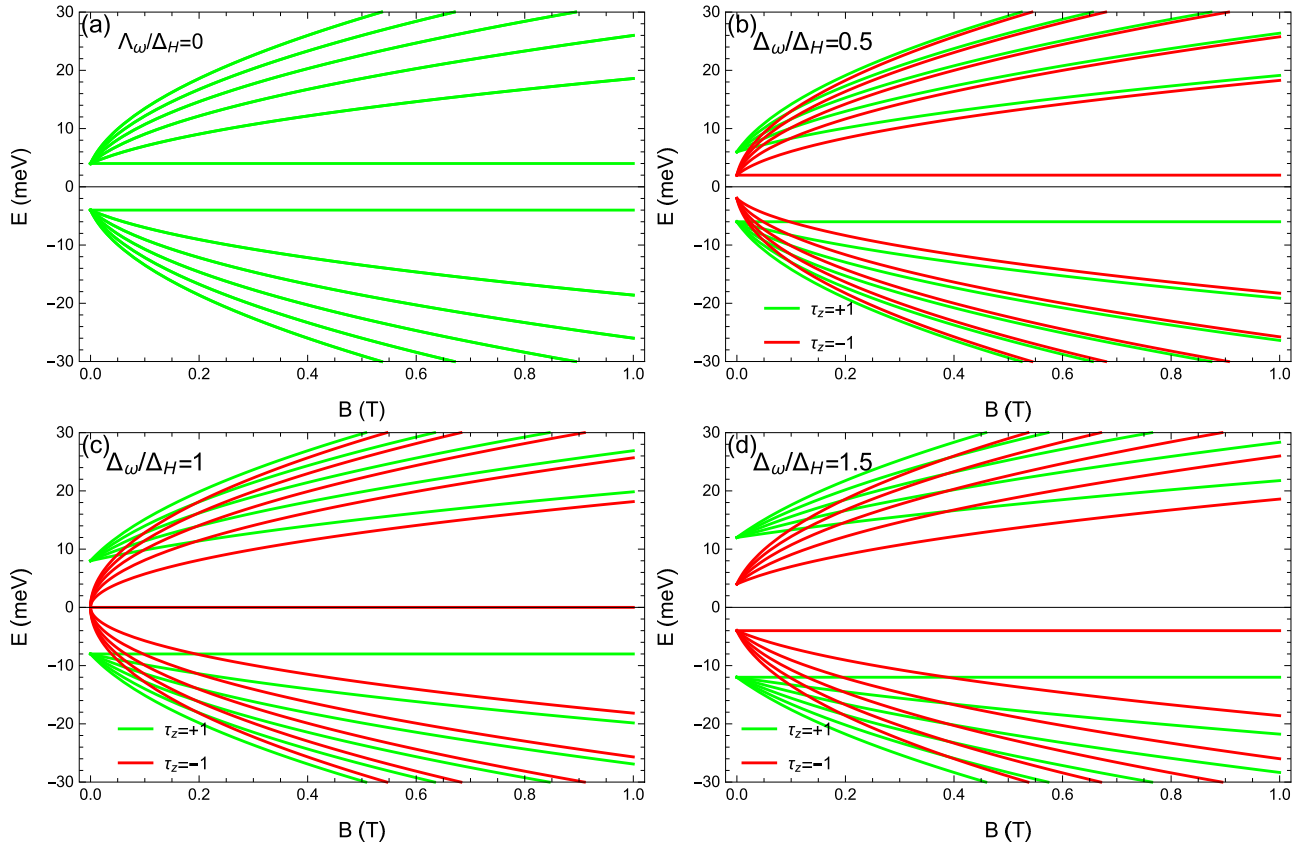


FIG. 2. The FTI thin-film LL energies versus magnetic-field B in distinct topological phases. (a) $\Lambda_\omega = 0$, (b) $\Lambda_\omega = 0.5\Delta_H$, (c) $\Lambda_\omega = \Delta_H$, and (d) $\Lambda_\omega = 1.5\Delta_H$. The top and bottom SS bands are represented by solid green and red curves, respectively.

where

$$\mathcal{A}_{n,\tau_z}^{\eta,\mu} = \sqrt{(\mathcal{E}_{n,\tau_z}^{\eta,\mu} + \Delta_{\tau_z}^\eta)/2\mathcal{E}_{n,\tau_z}^{\eta,\lambda}}, \quad (9)$$

and

$$\mathcal{B}_{n,\tau_z}^{\eta,\mu} = \sqrt{(\mathcal{E}_{n,\tau_z}^{\eta,\mu} - \Delta_{\tau_z}^\eta)/2\mathcal{E}_{n,\tau_z}^{\eta,\lambda}}, \quad (10)$$

where $|n\rangle$ denotes a Fock state of the simple harmonic oscillator. In Figs. 2(a)–2(d), we have plotted the Landau-level energy dispersion of the FTI thin film versus the magnetic field for the symmetric and antisymmetric SSs. The hybridization potential Δ_H between the symmetric and the antisymmetric SSs leads to spin splitting into an electron and holelike $n = 0$ LLs and lifts the degeneracy. The $n = 0$ Landau levels of the FTI thin film for the top and bottom SSs electrons are pinned at different points in the conduction and valance bands in distinct topological phases. In the absence of the optical field $\Lambda_\omega = 0$, the $n = 0$ energy LLs are degenerate as shown in Fig. 2(a). As we further increase the strength of the optical field, then the system is in the QPSHI phase ($\Lambda_\omega = 0.5\Delta_H$) as illustrated in Fig. 2(b). In the

QPSHI phase, the $n = 0$ LL of the bottom SS is located in the conduction band, whereas the top SS is in the valance band. In the CNP state ($\Lambda_\omega = \Delta_H$), the gap of one of the bottom SS bands closes, and the $n = 0$ bottom SS Landau level sits at zero energy, whereas the $n = 0$ top SS Landau level is at negative energy, which exhibits graphenelike behavior [31] as depicted in Fig. 2(c). In the P-QHI state, the lowest-energy gap reopens, and the locations of the $n = 0$ Landau levels shift to the valance band as shown in Fig. 2(d). An opposite behavior can be identified by changing the light polarization from the RHCP to the LHCP.

B. Magneto-optical conductivities of Floquet topological insulators

With the knowledge of the Landau levels and eigenfunctions of the FTI thin film under the application of magnetic field, the SS-dependent magneto-optical conductivity can now be determined. The standard Kubo formalism is utilized to derive the expressions for the magneto-optical conductivity of the FTI thin film by taking into account the optical, magnetic fields, and frequency dependence. The general expression of the Kubo formula is [31,36,49] as follows:

$$\sigma_{\mu\nu}(i\omega, B) = \frac{i\hbar}{2\pi l_B^2} \sum_{\gamma, \tau_z = \pm 1} \sum_{mn} \frac{f_n - f_m}{\mathcal{E}_n - \mathcal{E}_m} \frac{\langle \Phi_{n,\tau_z}^{\eta,\lambda} | \hat{j}_\mu | \Phi_{m,\tau_z'}^{\eta',\lambda'} \rangle \langle \Phi_{m,\tau_z'}^{\eta',\lambda'} | \hat{j}_\nu | \Phi_{n,\tau_z}^{\eta,\lambda} \rangle}{\hbar\omega - (\mathcal{E}_n - \mathcal{E}_m) + i\Gamma}, \quad (11)$$

where $l_B = \sqrt{\hbar/eB}$ denotes the magnetic length, the Fermi-Dirac distribution function is represented by $f_n = 1/(1 + e^{(\mathcal{E}_n - \mu_F)/k_B T})$, μ_F is the chemical potential, $\hat{j}_{\mu/\nu}$ is the current density operator, and Γ is the phenomenological transport scattering rate. Evaluating the current density matrix elements explicitly gives

$$\sigma_{xx}(i\omega, B) = \frac{i\hbar e^2 v_F^2}{2\pi l_B^2} \sum_{\eta, \tau_z = \pm 1} \sum_{m,n} \frac{f_n - f_m}{\mathcal{E}_n - \mathcal{E}_m} \frac{(\mathcal{A}_{m, \tau_z}^{\eta', \lambda'} \mathcal{B}_{n, \tau_z}^{\eta, \lambda})^2 \delta_{m-1, n} + (\mathcal{B}_{m, \tau_z}^{\eta', \lambda'} \mathcal{A}_{n, \tau_z}^{\eta, \lambda})^2 \delta_{m+1, n}}{\hbar\omega - (\mathcal{E}_n - \mathcal{E}_m) + i\Gamma}. \quad (12)$$

The real and imaginary components of the longitudinal magneto-optical conductivity are given by

$$\frac{\text{Re}[\sigma_{xx}(\omega, B)]}{\sigma_0} = \frac{E_B^2}{\pi} \sum_{\eta, \tau_z = \pm 1} \sum_{m,n} \frac{f_n - f_m}{\mathcal{E}_n - \mathcal{E}_m} [(\mathcal{A}_{m, \tau_z}^{\eta', \lambda'} \mathcal{B}_{n, \tau_z}^{\eta, \lambda})^2 \delta_{m-1, n} + (\mathcal{B}_{m, \tau_z}^{\eta', \lambda'} \mathcal{A}_{n, \tau_z}^{\eta, \lambda})^2] \mathcal{M}_{mn}, \quad (13)$$

and

$$\frac{\text{Im}[\sigma_{xx}(\omega, B)]}{\sigma_0} = \frac{E_B^2}{\pi} \sum_{\eta, \tau_z = \pm 1} \sum_{m,n} \frac{f_n - f_m}{\mathcal{E}_n - \mathcal{E}_m} [(\mathcal{A}_{m, \tau_z}^{\eta', \lambda'} \mathcal{B}_{n, \tau_z}^{\eta, \lambda})^2 \delta_{m-1, n} + (\mathcal{B}_{m, \tau_z}^{\eta', \lambda'} \mathcal{A}_{n, \tau_z}^{\eta, \lambda})^2] \mathcal{M}'_{mn}, \quad (14)$$

respectively. Here, $\sigma_0 = e^2/4\hbar$ being the universal conductivity, $\mathcal{M}_{mn} = \Gamma/[\hbar\omega - (\mathcal{E}_n - \mathcal{E}_m)]^2 + \Gamma^2$ and $\mathcal{M}'_{mn} = [\hbar\omega - (\mathcal{E}_n - \mathcal{E}_m)]/[\hbar\omega - (\mathcal{E}_n - \mathcal{E}_m)]^2 + \Gamma^2$. Similarly, the real and imaginary components of the transverse Hall conductivity can be obtained as

$$\frac{\text{Re}[\sigma_{xy}(\omega, B)]}{\sigma_0} = \frac{E_B^2}{\pi} \sum_{\eta, \tau_z = \pm 1} \sum_{m,n} \frac{f_n - f_m}{\mathcal{E}_n - \mathcal{E}_m} [(\mathcal{A}_{m, \tau_z}^{\eta', \lambda'} \mathcal{B}_{n, \tau_z}^{\eta, \lambda})^2 \delta_{m-1, n} - (\mathcal{B}_{m, \tau_z}^{\eta', \lambda'} \mathcal{A}_{n, \tau_z}^{\eta, \lambda})^2] \mathcal{M}'_{mn}. \quad (15)$$

and

$$\frac{\text{Im}[\sigma_{xy}(\omega, B)]}{\sigma_0} = \frac{E_B^2}{\pi} \sum_{\eta, \tau_z = \pm 1} \sum_{m,n} \frac{f_n - f_m}{\mathcal{E}_n - \mathcal{E}_m} [(\mathcal{A}_{m, \tau_z}^{\eta', \lambda'} \mathcal{B}_{n, \tau_z}^{\eta, \lambda})^2 \delta_{m-1, n} - (\mathcal{B}_{m, \tau_z}^{\eta', \lambda'} \mathcal{A}_{n, \tau_z}^{\eta, \lambda})^2] \mathcal{M}_{mn}. \quad (16)$$

In the limit, $\Lambda_\omega = \Delta_H = 0$, the magneto-optical conductivities of the monolayer graphene are recovered [31].

III. RESULTS AND DISCUSSIONS

A. Influence of off-resonant circularly polarized laser field: Transition from the QPSHI to the P-QHI phase

To better understand the SS-dependent MO conductivities of the FTI thin film, we discuss the numerical results here. Landau-level energies as a function of the applied magnetic field of the FTI thin film are depicted in Figs. 3(a) and 3(b) for RHCP and LHCP irradiated light, respectively. We have drawn the allowed LLs transitions for $B = 1$ T in the QPSHI phase. In Figs. 3(c)–3(f), we have shown the real components of the longitudinal and Hall conductivities as a function of photon energy in the QPSHI phase for the symmetric and antisymmetric SSs. We have chosen $\Lambda_\omega = 2$, $\Delta_H = 4$ [50], $\mu_F = 0$ meV, $B = 1$ T, and $\Gamma = 0.15\Delta_H$ [51] parameters for these simulations. In Fig. 3(c), we can observe resonant absorptive peaks in σ_{xx} spectra when the incident photon with energy $\hbar\omega$ matches the gap between the two LLs. The dotted shaded green curve is for the bottom SS electron and the solid red shaded curve is for the top SS electron transitions. The resonant features corresponding to different optical transitions $\mathcal{E}_m^{\tau_z = \pm 1} \rightarrow \mathcal{E}_n^{\tau_z = \pm 1}$ are labeled as $T_{mn}^{\tau_z = \pm 1}$, and these transitions are drawn in Fig. 3(a). We can observe a series of absorptive peaks in σ_{xx} where each of these peaks is represented by a Lorentzian peak. For example, the first two absorptive peaks in the upper panel of Fig. 3(c) correspond to the T_{01}^{-1} (bottom surface) and the T_{-10}^{+1} (top surface) transitions, which are the transitions from $n = 0$ to $n = 1$ Landau levels

as depicted in Fig. 3(b). Here, optically allowed interband Landau-level optical transitions satisfying the selection rule $|m| = |n \pm 1|$ for the symmetric and antisymmetric SSs. The spectral weights or areas of the bottom SS absorption peak are larger than the top SS peak. The other peaks at higher magneto-excitation energies originate from T_{-12}^{-1} , T_{-12}^{+1} , T_{-21}^{-1} , and T_{-21}^{+1} transitions, respectively. All the peaks gradually shift towards higher magneto-excitation frequencies with reduced spectral weights. Next, we calculate the real component of the Hall conductivity as a function of $\hbar\omega$ in Fig. 3(d). The main characteristics of the real part of the transverse Hall conductivity are its antisymmetric nature about its zero value. We can see the first positive (negative) and negative (positive) peaks at $\hbar\omega = 20.3$ and $\hbar\omega = 25.12$ meV, for top (bottom) SSs, respectively. These peaks in the conductivity spectra result from $n = 0$ to $n = 1$ LLs transitions. The other pairs of positive and negative peaks can be seen at higher magneto-excitation energies for T_{-12}^{-1} , T_{-12}^{+1} , T_{-21}^{-1} , and T_{-21}^{+1} transitions. We have plotted the real components of the surface state-dependent longitudinal and Hall conductivities of the FTI thin film for the LHCP irradiated light in Figs. 3(e) and 3(f). Reversing the optical field polarization from the RHCP to the LHCP leads to an exchange of SSs in both the valence and the conduction bands as shown in Fig. 3(b).

An irradiated off-resonant optical field Λ_ω , controls the electronic band structure of the TI as illustrated in Figs. 2(a)–2(d). Here, we use an alternative approach to understand the interplay between the surface state-dependent MO conductivities and the TQPTs in the FTI thin film. We plotted the real part of the longitudinal and imaginary parts of the transverse Hall conductivity as a function of

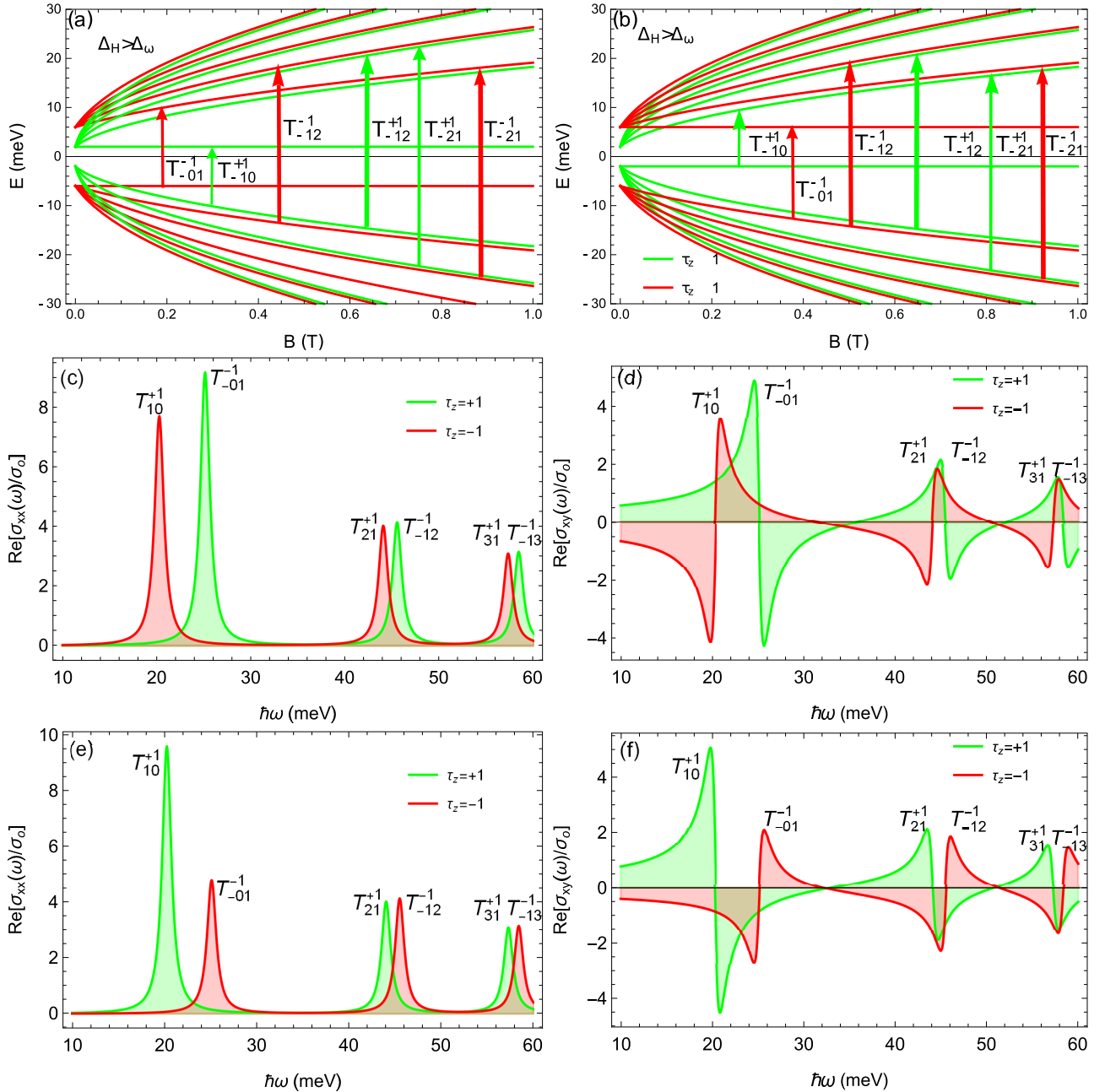


FIG. 3. Landau-level dispersion of the FTI thin film versus applied magnetic field for (a) RHCP and (b) LHCP irradiated light. (c) The real components of the longitudinal and (d) transverse Hall conductivity for RHCP light at $B = 1$ T and $\mu_F = 0$ meV in the QPSHI phase. (e) The real part of longitudinal and (f) transverse Hall conductivity for LHCP light at $B = 1$ T and $\mu_F = 0$ meV in the QPSHI phase. The top and bottom SSs conductivities are represented by solid shaded green and red curves, respectively.

normalized optical field Λ_ω/Δ_H and photonic energies $\hbar\omega/\Delta_H$ in Figs. 4(a) and 4(b). The CNP state appears at the critical point between the QPSHI and the P-QHI phases as shown in Fig. 4(a) for $B = 1$ T and $\mu_F = 0$ meV. Figure 4(b) depicts the imaginary part of the transverse Hall conductivity as a function of the normalized optical field and photonic energies. At critical point, the sign of the conductivity peaks switches which indicates a QPT. From Figs. 4(a) and 4(b), it is clear that the optical transitions caused by the $n=0$ Landau levels scale nearly linearly for different optical fields, whereas the other optical transitions approximately parabolically.

In the following, we explore the real parts of the surface state-dependent magneto-optical conductivities of the FTI thin film in distinct topological phases. The absorptive part of the longitudinal conductivity versus the photon energy is shown in Fig. 4(c) for varying Λ_ω whereas keeping $\mu_F = 0$ meV and $B = 1$ T for the RHCP light. From the top panel of Fig. 4(c), it is clear that as the intensity of the laser field Λ_ω is increased, each interband transition splits into two transitions corresponding to the symmetric and antisymmetric SSs. In the QPSHI regime ($\Lambda_\omega = 0.5\Delta_H$), the first and second absorption peaks originate from the T_{-10}^{+1} and

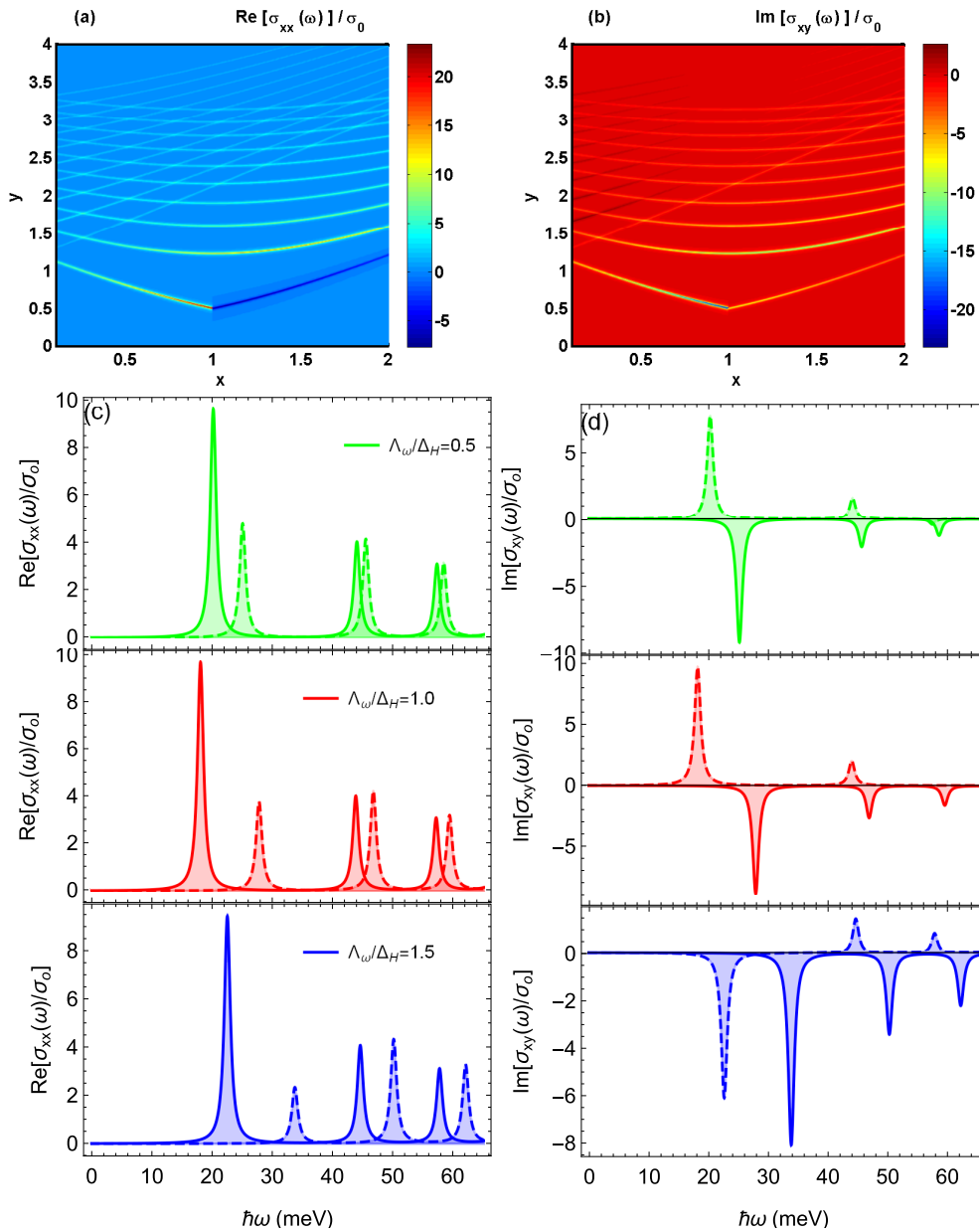


FIG. 4. (a) The real component of the longitudinal and (b) the imaginary component of the Hall magneto-optical conductivity for $B = 1$ T and $\mu_F = 0$ meV in distinct topological phases. (c) The real component of the longitudinal and (d) the imaginary component of the Hall magneto-optical conductivity as a function of normalized optical field ($x = \Lambda_\omega/\Delta_H$) and photonic energies ($y = \hbar\omega/\Delta_H$) for $B = 1$ T and $\mu_F = 0$ meV in distinct topological phases. The top (bottom) SS-dependent conductivities are represented by solid (dotted) shaded curves, respectively.

T_{-01}^{-1} transitions. In each of these optical transitions, one of the participating levels is an $n = 0$ level. The spectral weight of the top SS peak is larger compared to the bottom SS. In the CNP state ($\Lambda_\omega/\Delta_H = 1$), the first two transitions originated from the $n = 0$ to $n = 1$ LLs move apart: the T_{-10}^{+1} (T_{-01}^{-1}) absorptive peak is red- (blue)shifted, which shows that the top SS electron band gap closes as shown in the middle panel of Fig. 4(c). In this state, the magneto-excitation energies corresponding to the first and second absorption peaks are 18.2 and 27.8 meV, respectively. For $\Lambda_\omega > \Delta_H$, the system is in the P-QHI regime. Due to the lowest gap reopening, all interband transition magneto-excitation energies move to

higher energy in this regime as presented in the lower panel of Fig. 4(c). To fully understand the SS-dependent MO absorption spectra of the Hall conductivity, we show the imaginary component of the Hall conductivity with photon energy in Fig. 4(d) in distinct topological regimes for the RHCP light. For $\Lambda_\omega = 0.5\Delta_H$, the imaginary component of the σ_{xy} only shows a positive (negative) peak for the top and bottom SS transitions as depicted in the top panel of Fig. 4(d). In the CNP state, we can observe a similar trend as shown in the QPSHI phase, but the bottom (top) SS transition excitation energies are moving to the right (left). The spectral weights of the absorption peaks are also enhanced in the CNP state

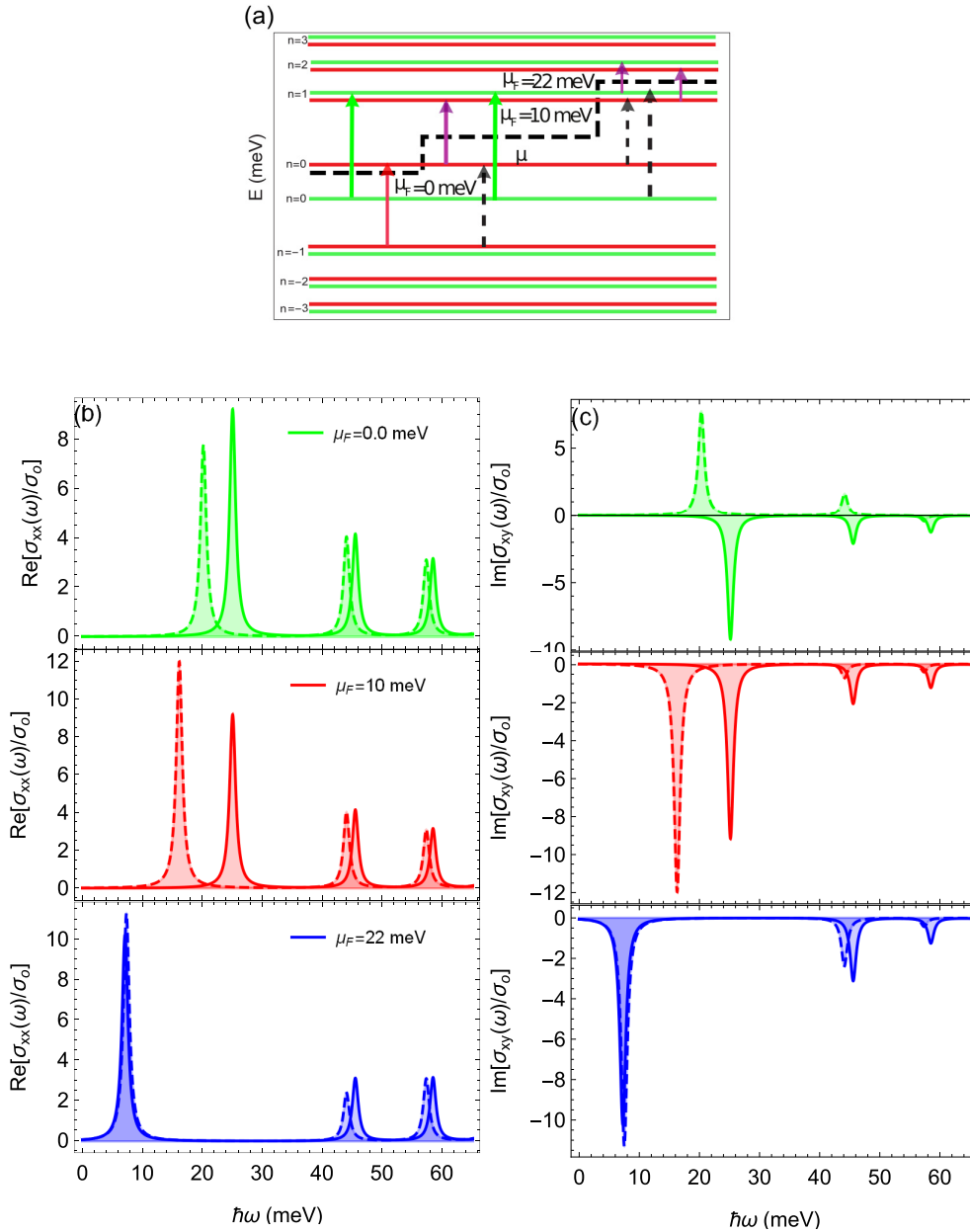


FIG. 5. (a) Schematic representation of optically allowed Landau-level transitions for the symmetric and antisymmetric SSs in the QPSHI phase for three different values of electron concentrations subjected to selection rules. The longitudinal conductivity and Hall conductivity versus photon energy for different chemical potentials. (b) The real component of longitudinal and (c) the imaginary component of the Hall magneto-optical conductivity as a function of photonic energy for $B = 1$ T. The top (bottom) SS-dependent conductivities are represented by solid (dotted) shaded curves, respectively.

as depicted in the middle portion of Fig. 4(d). In the P-QHI phase, both of the absorptive peaks originating from the $n = 0$ to $n = 1$ Landau-level transitions are negative as presented in the lower panel of Fig. 4(d). The spectral weight of the top SS transition is larger than the bottom SS transition.

B. Chemical potential dependence on the magneto-optical conductivity of Floquet topological insulators

We now examine how the chemical potential μ_F affects the magneto-optical conductivities of the Floquet topological insulator thin film. The electron densities in the FTI thin film

can be tuned by using external bias or by optical pumping. In Fig. 5(a), we have shown the energy dispersion of the FTI thin film with magnetic-field B for allowed and forbidden (Pauli blocked) optical transitions. We have chosen three different values of electron densities or chemical potentials for $B = 1$ T in the QPSHI phase for the LHCP light, respectively. In the first case, we consider $\mu_F = 0$ meV and falls within the $n = 0$ Landau levels. In the second case, μ_F is varied, and it moves to $\mu_F = 10$ meV where it falls between the $n = 0$ and the $n = 1$ Landau levels. In the third case, we have chosen $\mu_F = 22$ meV, and it is residing in between the $n = 1$ and the $n = 2$ Landau levels. For $\mu_F = 0$, we have pure interband transitions

for the symmetric and antisymmetric SSs as depicted in the top panel of Fig. 5(b). These interband transitions for the symmetric and antisymmetric SSs are presented by green and red arrows, respectively, in Fig. 5(a). They identify as $T_{-10}^{-1} = 20.3$ and $T_{10}^{+1} = 25.1$ meV for the symmetric and antisymmetric SSs respectively in Fig. 5(b). The intensity of the first peak is smaller, which is associated entirely with bottom SS electrons compared to the top SS peak. Including a finite chemical potential $\mu_F = 10$ meV, causes various LL transitions to become Pauli blocked. For example, the optical transition originating from bottom SS $T_{-10}^{-1} = 20.3$ meV becomes Pauli blocked (shown by black dashed arrow) and, in its stead, the intraband Landau-level transition $T_{01}^{-1} = 16.0$ meV appears, whereas for the top SS electron, we can see the allowed interband LL transition $T_{01}^{+1} = 25.1$ meV. The intraband and Pauli-blocked optical transitions are shown by purple and black dashed upward pointing arrows in Fig. 5(a). The lowest interband peak redistributes its intensity between itself and an intraband peak as depicted in the middle panel of Fig. 5(b). These intraband transitions result entirely from bottom SS electrons, whereas the second peak is associated entirely with top SS electrons. The spectral weight of the second interband peak reduces as compared to the intraband transitions.

In the third case, μ_F is sitting between the $n = 1$ and the $n = 2$ Landau levels, both interband transitions starting from $n = 0$, i.e., T_{-10}^{-1} and T_{01}^{+1} now disappear due to Pauli blocking. These Pauli-blocked optical Landau-level transitions are again presented by the dashed arrows in the rightmost part of Fig. 5(a). In their place, however, the intraband optical transitions (shown by purple arrows) arise. It is worth mentioning that for different chemical potentials, some of the optical features are strong, whereas others are weak as shown in Fig. 5(b). We also observe that the intraband transitions in the lower portion of Fig. 5(b) are closely spaced. We note that the transitions involving the $n = 0$ Landau levels of the bottom and top SSs completely disappeared from the conductivity spectrum. We can see that the intensity of the next peak is reduced as interband transitions to the $n = 1$ Landau levels are forbidden and Pauli blocked as presented by the black-dashed arrows in Fig. 5(b). Note that the peaks corresponding to higher-energy Landau-level optical transitions are not affected by the variation of the chemical potentials.

We now consider the absorptive component of the imaginary magneto-optical Hall conductivity for different chemical potentials. Figure 5(c) presents the imaginary absorptive component of the magneto-optical transverse Hall conductivity with photon energy in a magnetic-field $B = 1$ T. In the upper panels, μ_F is taken to be zero meV. It is clear from Fig. 5(c) that the positive and negative peaks corresponding to T_{-10}^{-1} and T_{01}^{+1} , respectively. The transitions originating from the $n = 1$ and $n = 2$ Landau levels (T_{-12}^{-1} , T_{-21}^{-1} , T_{-21}^{+1} , and T_{-21}^{+1}). The magnitude of $n = 1$ and $n = 2$ Landau-level peaks is fewer than those for $n = 0$ and $n = 1$ Landau levels as shown in the top panel of Fig. 5(c). For $\mu_F = 10$ meV, we can see an absorptive intraband and interband features for the lowest-energy transitions for the bottom and top SSs, respectively, as depicted in the middle portion of Fig. 5(c). With increased $\mu_F = 22$ meV, the spectral weight of bottom and top SSs interband transitions is redistributed to a single strong intraband

peak. We observe that the intraband transition peaks of the imaginary absorptive component of the Hall conductivity are redshifted with the increase in the doping due to the decreasing Landau-level spacings as depicted in the bottom panel of Fig. 5(c).

C. Faraday and Kerr effects in Floquet topological insulators

In this section, we demonstrate the Faraday and Kerr effects in the FTI thin film when subjected to an external off-resonant optical and magnetic fields. We consider an ultrathin film of the Floquet topological insulator (such that $d \rightarrow 0$). In these situations, the FTI thin-film top and bottom surface states can be treated as two-dimensional surfaces as far as light-matter interaction is concerned. We consider a linearly polarized light beam interacting with the Floquet topological insulator thin-film-substrate system with an incidence angle θ_1 . In this scenario, a linearly polarized electromagnetic beam of frequency ω is propagating through the FTI thin film. The Fresnel reflection and transmission coefficients under the influence of a magnetic-field B of a two-dimensional material can be computed by using Maxwell's equations and matching the appropriate electromagnetic boundary conditions on either side of the FTI thin film [36,49],

$$r_{pp}(\mathbf{k}, i\omega, B) = \frac{\Sigma_+^T \Sigma_-^L + Z_0^2 \mu_1 \mu_2 q_{1z} q_{2z} \sigma_{xy}^2(i\omega, B)}{\Sigma_+^T \Sigma_+^L + Z_0^2 \mu_1 \mu_2 q_{1z} q_{2z} \sigma_{xy}^2(i\omega, B)}, \quad (17)$$

$$r_{ss}(\mathbf{k}, i\omega, B) = -\frac{\Sigma_-^T \Sigma_+^L + Z_0^2 \mu_1 \mu_2 q_{1z} q_{2z} \sigma_{xy}^2(i\omega, B)}{\Sigma_+^T \Sigma_+^L + Z_0^2 \mu_1 \mu_2 q_{1z} q_{2z} \sigma_{xy}^2(i\omega, B)}, \quad (18)$$

$$t_{pp}(\mathbf{k}, i\omega, B) = 2 \frac{Z_2 \varepsilon_2}{Z_1} \frac{q_{1z} \Sigma_+^T}{\Sigma_+^T \Sigma_+^L + Z_0^2 \mu_1 \mu_2 q_{1z} q_{2z} \sigma_{xy}^2(i\omega, B)}, \quad (19)$$

$$t_{ss}(\mathbf{k}, i\omega, B) = 2\mu_2 \frac{q_{1z} \Sigma_+^L}{\Sigma_+^T \Sigma_+^L + Z_0^2 \mu_1 \mu_2 q_{1z} q_{2z} \sigma_{xy}^2(i\omega, B)}, \quad (20)$$

$$\begin{aligned} r_{sp}(\mathbf{k}, i\omega, B) &= t_{sp}(\mathbf{k}, i\omega, B) \\ &= \frac{-2Z_0^2 \mu_0 \mu_1 \mu_2 q_{1z} q_{2z} \sigma_{xy}(i\omega, B)}{Z_1 [\Sigma_+^T \Sigma_+^L + Z_0^2 \mu_1 \mu_2 q_{1z} q_{2z} \sigma_{xy}^2(i\omega, B)]}, \end{aligned} \quad (21)$$

$$\begin{aligned} r_{ps}(\mathbf{k}, i\omega, B) &= -\frac{k_1 q_{2z}}{k_2 q_{1z}} t_{ps}(\mathbf{k}, i\omega, B) \\ &= -2 \frac{Z_0^2 \mu_1 \mu_2}{Z_1} \\ &\quad \times \frac{q_{1z} q_{2z} \sigma_{xy}(i\omega, B)}{\Sigma_+^T \Sigma_+^L + Z_0^2 \mu_1 \mu_2 q_{1z} q_{2z} \sigma_{xy}^2(i\omega, B)}, \end{aligned} \quad (22)$$

where

$$\Sigma_{\pm}^L = [q_{1z} \varepsilon_2 \pm q_{2z} \varepsilon_1 + q_{1z} q_{2z} \sigma_{xx}(i\omega, B)] / (\varepsilon_0 \omega), \quad (23)$$

$$\Sigma_{\pm}^T = [q_{2z} \mu_1 \pm q_{1z} \mu_2 + \mu_0 \mu_1 \mu_2 \sigma_{xy}(i\omega, B) \omega]. \quad (24)$$

Here, we denoted the permittivity and permeability of the media by ε_n and μ_n , respectively, and impedances by $Z_n = Z_0 \sqrt{\mu_n / \varepsilon_n}$ and $Z_0 = \sqrt{\mu_0 / \varepsilon_0}$ where $n = (1, 2)$. The

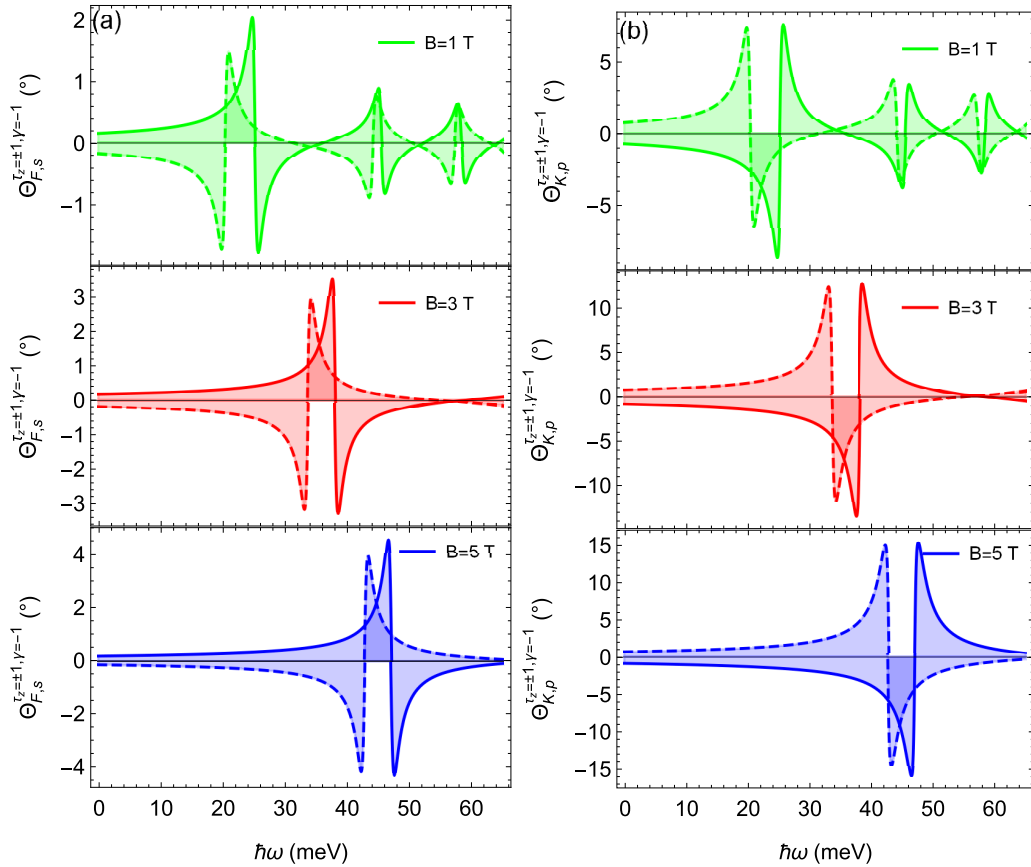


FIG. 6. (a) The s -polarized Faraday rotation for different magnetic fields and (b) p -polarized Kerr rotations in the QPSH phase ($\Lambda_\omega = 0.5\Delta_H$) for different magnetic fields for the RHCP light. The top and bottom SS conductivities are represented by solid and dotted shaded curves, respectively. The parameters chosen are $\Gamma = 0.15\Delta_H$ and $\theta_1 = 45^\circ$.

incident and transmitted wave vectors are represented by $q_{1z} = k_1 \cos(\theta_1)$ and $q_{2z} = k_2 \cos(\theta_2)$, respectively. For the FTI thin-film substrate system, we consider $\varepsilon_1 = 1$ and $\mu_1 = 1$ for medium 1 and $\mu_2 = 1$ for medium 2 (nonmagnetic). The reflection and transmission coefficients, which are strongly dependent on the surface state-dependent MO conductivities, subsequently, determine the Faraday and Kerr rotations. The Faraday and Kerr rotation angles for the incident s - and p -polarized beam can be written as

$$\Theta_{F,s}^{\tau_z=\pm 1, \gamma=1} = \frac{1}{2} \tan^{-1} \left(2 \frac{\text{Re}(\chi_F^{s(p)})}{1 - |\chi_F^{s(p)}|^2} \right), \quad (25)$$

$$\Theta_{K,s(p)}^{\tau_z=\pm 1, \gamma=1} = \frac{1}{2} \tan^{-1} \left(2 \frac{\text{Re}(\chi_K^{s(p)})}{1 - |\chi_K^{s(p)}|^2} \right), \quad (26)$$

where $\chi_F^s = t_{ps}/t_{ss}$, $\chi_F^p = t_{sp}/t_{pp}$, $\chi_K^s = r_{ps}/r_{ss}$, and $\chi_K^p = r_{sp}/r_{pp}$. In the next section, we calculate the Faraday and Kerr rotations of the transmitted and reflected lights by using Eqs. (25) and (26).

We first demonstrate the magnetic-field modulated Faraday and Kerr rotation angles as a function of $\hbar\omega$ in the FTI thin film for $\mu_F = 0$ meV in the QPSHI phase. In Figs. 6(a) and 6(b), we plot $\Theta_{F,s}^{\tau_z=\pm 1, \gamma=1}$ and $\Theta_{K,p}^{\tau_z=\pm 1, \gamma=1}$ at $B = 1, 3,$ and 5 T shown in the upper, middle, and lower panels of Figs. 6(a) and 6(b) respectively. We have presented the s -polarized

Faraday rotation versus photonic energy for the RHCP light in the top panel of Fig. 6(a). The Floquet topological insulator thin-film Landau-level dispersion is strongly dependent on the perpendicularly applied magnetic field as obvious by Eq. (5). The Faraday rotation signal originating from any SS is dispersive Lorentzian. We can observe a positive (negative) Lorentzian followed by a negative (positive) signal for the symmetric and antisymmetric SSs of the FTI thin film, respectively. We can call this dispersive Lorentzian an antiphase peak. The Faraday rotation angle for the first two antiphase peaks is $\sim \pm 2^\circ$ and $\sim \pm 1.5^\circ$ for both SSs at $B = 1$ T, respectively. A discernible Faraday rotation antiphase peaks for both SSs are also observed at higher magnetoexcitation terahertz (THz) frequencies with a maximum value of Faraday rotation angle $\sim \pm 0.8^\circ$. For larger values of the B field, the magneto-optic excitation energies shift towards the right (i.e., towards higher-THz frequencies) with a consequent increase in the amount of the Faraday rotation angle $\Theta_{F,s}^{\tau_z=\pm 1, \gamma=1}$. For example, the maximum value of the rotation $\Theta_{F,s}^{\tau_z=\pm 1, \gamma=1} = \pm 4.4^\circ$ at $B = 5$ T, which is really a large amount of rotation compared to previous work on Bi_2Se_3 TIs [52,53]. The externally applied magnetic field only shifts the position of the photonic energies, which also modifies the magnitude of the Faraday rotation angle. Figure 6(b) illustrates the p -polarized magneto-optical Kerr effect spectra versus photonic energy for both SSs in the QPSHI phase for different magnetic fields.

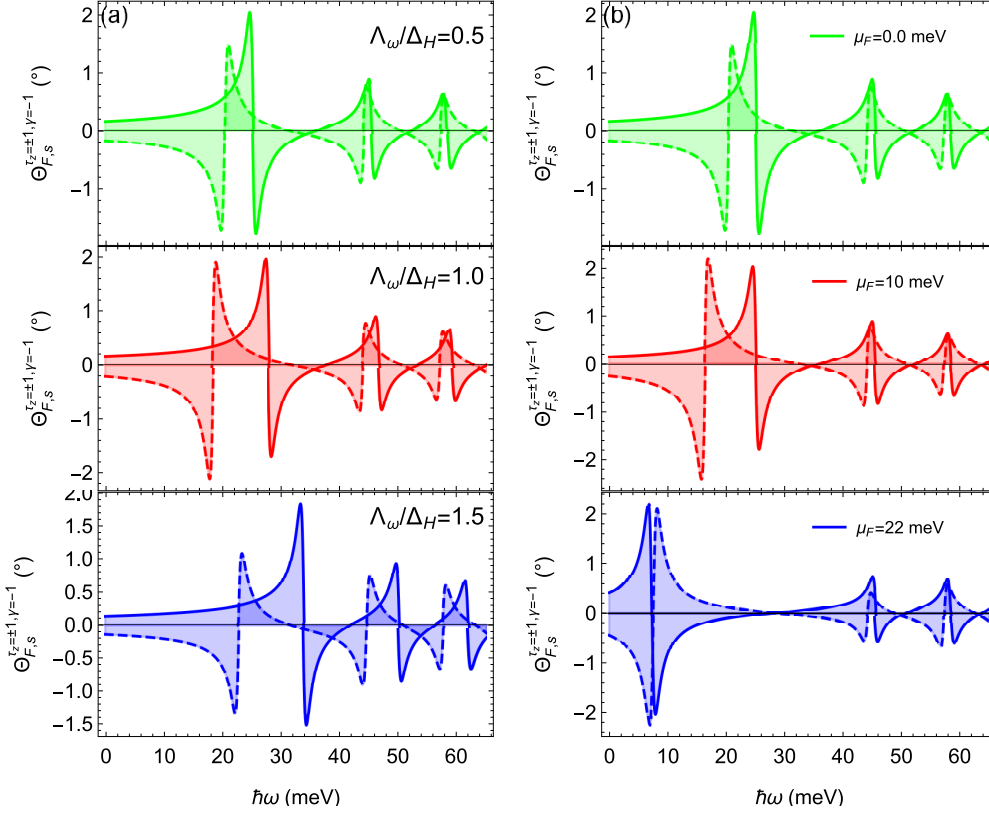


FIG. 7. (a) The s -polarized Faraday rotation with $\hbar\omega$ in distinct topological phases and (b) s -polarized Faraday rotation versus photon energy for different chemical potentials in the QPSH phase for the RHCP light. The top and bottom SSs conductivities are represented by solid and dotted shaded curves, respectively. The parameters used are $B = 1$ T, $\theta_1 = 45^\circ$, $\Gamma = 0.15\Delta_H$, and refractive index $n_2 = 1.84$.

We noted that the giant Kerr rotations are originating from the first two antiphase peaks (T_{-01}^{-1} and T_{-10}^{+1} transitions). On the other hand, we can observe a relatively small Kerr rotation antiphase peaks corresponding to second and third magneto-excitation transitions (T_{-12}^{-1} , T_{-12}^{+1} , T_{-21}^{-1} , and T_{-21}^{+1}). For $B = 5$ T (see the bottom panel), the Kerr rotation angle reaches $\Theta_{K,p}^{\tau_z=\pm 1, \gamma=1} = \pm 15^\circ$.

Figure 7(a) represents the Faraday rotation versus photon energy $\hbar\omega$ for different off-resonant optical fields in the THz regime at $B = 1$ T, whereas keeping $\mu_F = 0$. In the upper panel of Fig. 6(a), we already explained the Faraday rotation in the QPSHI regime ($\Lambda_\omega = 0.5\Delta_H$). In the middle panel of Fig. 6(a), we plot the SS-dependent Faraday rotation with photonic energy in the CNP state. The magnitude of surface state-dependent Faraday angles for both QPSHI and CNP states are $\approx \pm 2.0^\circ$ for both SSs transitions. In the P-QHI phase ($\Lambda_\omega/\Delta_H = 1.5$), the antiphase pair is blueshifted as shown in the lower panel of Fig. 6(a). Here, the amount of the Faraday rotation is relatively small as compared to the QPSHI and CNP states. In the subsequent analysis, we examine how doping affects the Faraday rotation angle. Recent experiments have demonstrated that the Landau levels of the FTI thin film can be adjusted by employing back and topgate electrodes [54,55]. The s -polarized Faraday rotation angles are shown in Fig. 7(b) for different chemical potentials. The top panel of Fig. 7(b) presents the Faraday rotation for $\mu_F = 0$ meV, which is originating from purely interband transitions. The Faraday rotation angle for the top SS is larger

compared to the bottom SS transition. As we increase $\mu_F = 10$ meV, we observe that the maximum Faraday rotation is achieved at the bottom SS as depicted in the middle panel of Fig. 7(b). This large rotation is due to the intraband ($T_{01}^{-1} = 16.3$ -meV) transition. For $\mu_F = 22$ meV, these Faraday rotation signatures originate from the two intraband transitions $T_{12}^{+1} = 7.2$ and $T_{12}^{-1} = 7.5$ meV as illustrated in the bottom portion of Fig. 7(b). We further note that the top and bottom SS antiphase peaks switch signs, which show the modulation of the Faraday rotation angle by switching the chemical potential. The Faraday rotation angle is enhanced due to the intraband transitions.

IV. CONCLUSION

We have computed the Landau-level energy dispersion and magneto-optical conductivity of the FTI thin-film system based on linear-response theory. We discussed the energy dispersion of the FTI thin film with and without magnetic field in distinct topological phases. We derived analytic expressions for the surface state-dependent MO conductivities of the Floquet topological insulator thin film for the LHCP- and RHCP-irradiated light. The surface state-dependent magneto-optical conductivity spectra reflect the structure of the Landau levels. By changing the intensity of the off-resonant laser field, the behavior of the longitudinal and transverse conductivities signature quantum phase transitions. We demonstrated that the magneto-optical conductivities are

hugely dependent on the intensity of the applied optical and magnetic fields. We further studied the magnetic, optical fields, and chemical potential-modulated surface states dependent on Faraday and Kerr rotations. We found that the amount of the maximum Faraday and Kerr rotation angles exceeds $\approx 4.4^\circ$ and $\approx 15^\circ$ for $B = 5$ T, respectively. Our simulation results shed light on the surface state-dependent magneto-optical effects of the FTI thin-film systems and open a promising route to design novel photonic, optoelectronics, and optospintronic devices.

ACKNOWLEDGMENTS

M.Z. and Y.M. acknowledge support from KAUST. M.Q.M. acknowledges visit support from Innovative Technologies Laboratories (ITL), KAUST. Y.S.A. is supported by the Singapore University of Technology and Design Kickstarter Initiatives (SKI) under the Project No. SKI 2021_01_12. M.S. acknowledges the support received in part from Zhejiang Normal University under Grant No. YS304023905.

-
- [1] M. Z. Hasan and C. L. Kane, Colloquium: Topological insulators, *Rev. Mod. Phys.* **82**, 3045 (2010).
- [2] X.-L. Qi and S.-C. Zhang, Topological insulators and superconductors, *Rev. Mod. Phys.* **83**, 1057 (2011).
- [3] M. Kim, Z. Jacob, and J. Rho, Recent advances in 2D, 3D and higher-order topological photonics, *Light: Sci. Appl.* **9**, 1 (2020).
- [4] L. Cao, G. Zhou, Q. Wu, S. A. Yang, H. Y. Yang, Y. S. Ang, and L. K. Ang, Electrical Contact between an Ultrathin Topological Dirac Semimetal and a Two-Dimensional Material, *Phys. Rev. Appl.* **13**, 054030 (2020).
- [5] A. H. Castro Neto, F. Guinea, N. M. R. Peres, K. S. Novoselov, and A. K. Geim, The electronic properties of graphene, *Rev. Mod. Phys.* **81**, 109 (2009).
- [6] P. Roushan, J. Seo, C. V. Parker, Y. S. Hor, D. Hsieh, D. Qian, A. Richardella, M. Z. Hasan, R. J. Cava, and A. Yazdani, Topological surface states protected from backscattering by chiral spin texture, *Nature (London)* **460**, 1106 (2009).
- [7] D. Culcer, A. MacDonald, and Q. Niu, Anomalous hall effect in paramagnetic two-dimensional systems, *Phys. Rev. B* **68**, 045327 (2003).
- [8] F. D. M. Haldane, Model for a Quantum Hall Effect without Landau Levels: Condensed-Matter Realization of the Parity Anomaly, *Phys. Rev. Lett.* **61**, 2015 (1988).
- [9] C.-Z. Chang, J. Zhang, X. Feng, J. Shen, Z. Zhang, M. Guo, K. Li, Y. Ou, P. Wei, L.-L. Wang *et al.*, Experimental observation of the quantum anomalous hall effect in a magnetic topological insulator, *Science* **340**, 167 (2013).
- [10] X.-L. Qi, T. L. Hughes, and S.-C. Zhang, Topological field theory of time-reversal invariant insulators, *Phys. Rev. B* **78**, 195424 (2008).
- [11] A. M. Essin, J. E. Moore, and D. Vanderbilt, Magnetoelectric Polarizability and Axion Electrodynamics in Crystalline Insulators, *Phys. Rev. Lett.* **102**, 146805 (2009).
- [12] W.-K. Tse and A. H. MacDonald, Giant Magneto-Optical Kerr Effect and Universal Faraday Effect in Thin-Film Topological Insulators, *Phys. Rev. Lett.* **105**, 057401 (2010).
- [13] X.-L. Qi, R. Li, J. Zang, and S.-C. Zhang, Inducing a magnetic monopole with topological surface states, *Science* **323**, 1184 (2009).
- [14] J. H. Cullen, P. Bhalla, E. Marcellina, A. R. Hamilton, and D. Culcer, Generating a Topological Anomalous Hall Effect in a Nonmagnetic Conductor: An In-Plane Magnetic Field as a Direct Probe of the Berry Curvature, *Phys. Rev. Lett.* **126**, 256601 (2021).
- [15] J. E. Sipe and A. I. Shkrebtii, Second-order optical response in semiconductors, *Phys. Rev. B* **61**, 5337 (2000).
- [16] Y. Zhang, D. Huang, Y. Shan, T. Jiang, Z. Zhang, K. Liu, L. Shi, J. Cheng, J. E. Sipe, W.-T. Liu *et al.*, Doping-Induced Second-Harmonic Generation in Centrosymmetric Graphene from Quadrupole Response, *Phys. Rev. Lett.* **122**, 047401 (2019).
- [17] T. Morimoto and N. Nagaosa, Topological nature of nonlinear optical effects in solids, *Sci. Adv.* **2**, e1501524 (2016).
- [18] L. Wu, S. Patankar, T. Morimoto, N. L. Nair, E. Thewalt, A. Little, J. G. Analytis, J. E. Moore, and J. Orenstein, Giant anisotropic nonlinear optical response in transition metal monpnictide weyl semimetals, *Nat. Phys.* **13**, 350 (2017).
- [19] F. de Juan, A. G. Grushin, T. Morimoto, and J. E. Moore, Quantized circular photogalvanic effect in weyl semimetals, *Nat. Commun.* **8**, 15995 (2017).
- [20] Q. Ma, S.-Y. Xu, H. Shen, D. MacNeill, V. Fatemi, T.-R. Chang, A. M. Mier Valdivia, S. Wu, Z. Du, C.-H. Hsu *et al.*, Observation of the nonlinear hall effect under time-reversal-symmetric conditions, *Nature (London)* **565**, 337 (2019).
- [21] P. Bhalla, M.-X. Deng, R.-Q. Wang, L. Wang, and D. Culcer, Nonlinear Ballistic Response of Quantum Spin Hall Edge States, *Phys. Rev. Lett.* **127**, 206801 (2021).
- [22] P. Bhalla, A. H. MacDonald, and D. Culcer, Resonant Photovoltaic Effect in Doped Magnetic Semiconductors, *Phys. Rev. Lett.* **124**, 087402 (2020).
- [23] S. Singh, J. Kim, K. M. Rabe, and D. Vanderbilt, Engineering Weyl Phases and Nonlinear Hall Effects in T_d -MoTe₂, *Phys. Rev. Lett.* **125**, 046402 (2020).
- [24] C.-X. Liu, H. Zhang, B. Yan, X.-L. Qi, T. Frauenheim, X. Dai, Z. Fang, and S.-C. Zhang, Oscillatory crossover from two-dimensional to three-dimensional topological insulators, *Phys. Rev. B* **81**, 041307(R) (2010).
- [25] H.-Z. Lu, W.-Y. Shan, W. Yao, Q. Niu, and S.-Q. Shen, Massive dirac fermions and spin physics in an ultrathin film of topological insulator, *Phys. Rev. B* **81**, 115407 (2010).
- [26] J. L. Collins, A. Tadich, W. Wu, L. C. Gomes, J. N. Rodrigues, C. Liu, J. Hellerstedt, H. Ryu, S. Tang, S.-K. Mo *et al.*, Electric-field-tuned topological phase transition in ultrathin Na₃Bi, *Nature (London)* **564**, 390 (2018).
- [27] A. A. Zyuzin, M. D. Hook, and A. A. Burkov, Parallel magnetic field driven quantum phase transition in a thin topological insulator film, *Phys. Rev. B* **83**, 245428 (2011).
- [28] T. Kitagawa, T. Oka, A. Brataas, L. Fu, and E. Demler, Transport properties of nonequilibrium systems under the application

- of light: Photoinduced quantum hall insulators without landau levels, *Phys. Rev. B* **84**, 235108 (2011).
- [29] P. D. Sacramento, Charge and spin edge currents in two-dimensional floquet topological superconductors, *Phys. Rev. B* **91**, 214518 (2015).
- [30] V. Dal Lago, M. Atala, and L. E. F. Torres, Floquet topological transitions in a driven one-dimensional topological insulator, *Phys. Rev. A* **92**, 023624 (2015).
- [31] V. P. Gusynin and S. G. Sharapov, Unconventional Integer Quantum Hall Effect in Graphene, *Phys. Rev. Lett.* **95**, 146801 (2005).
- [32] A. Pound, J. P. Carbotte, and E. J. Nicol, Magneto-optical conductivity in graphene including electron-phonon coupling, *Phys. Rev. B* **85**, 125422 (2012).
- [33] K. S. Novoselov, Z. Jiang, Y. Zhang, S. Morozov, H. L. Stormer, U. Zeitler, J. Maan, G. Boebinger, P. Kim, and A. K. Geim, Room-temperature quantum hall effect in graphene, *Science* **315**, 1379 (2007).
- [34] P. Plochocka, C. Faugeras, M. Orlita, M. L. Sadowski, G. Martinez, M. Potemski, M. O. Goerbig, J.-N. Fuchs, C. Berger, and W. A. de Heer, High-Energy Limit of Massless Dirac Fermions in Multilayer Graphene using Magneto-Optical Transmission Spectroscopy, *Phys. Rev. Lett.* **100**, 087401 (2008).
- [35] C. J. Tabert and E. J. Nicol, Magneto-optical conductivity of silicene and other buckled honeycomb lattices, *Phys. Rev. B* **88**, 085434 (2013).
- [36] M. Shah and M. S. Anwar, Magneto-optical effects in the landau level manifold of 2D lattices with spin-orbit interaction, *Opt. Express* **27**, 23217 (2019).
- [37] R.-L. Chu, X. Li, S. Wu, Q. Niu, W. Yao, X. Xu, and C. Zhang, Valley-splitting and valley-dependent inter-landau-level optical transitions in monolayer MoS₂ quantum hall systems, *Phys. Rev. B* **90**, 045427 (2014).
- [38] M. Tahir, P. Vasilopoulos, and F. M. Peeters, Magneto-optical transport properties of monolayer phosphorene, *Phys. Rev. B* **92**, 045420 (2015).
- [39] A. Iurov, L. Zhemchuzhna, G. Gumbs, D. Huang, W.-K. Tse, K. Blaise, and C. Ejiogu, Floquet engineering of tilted and gapped dirac bandstructure in 1T' - MoS₂, *Sci. Rep.* **12**, 21348 (2022).
- [40] C. Bao, P. Tang, D. Sun, and S. Zhou, Light-induced emergent phenomena in 2D materials and topological materials, *Nat. Rev. Phys.* **4**, 33 (2022).
- [41] O. Kibis, Metal-insulator transition in graphene induced by circularly polarized photons, *Phys. Rev. B* **81**, 165433 (2010).
- [42] O. V. Kibis, K. Dini, I. V. Iorsh, and I. A. Shelykh, All-optical band engineering of gapped dirac materials, *Phys. Rev. B* **95**, 125401 (2017).
- [43] S. Morina, O. V. Kibis, A. A. Pervishko, and I. A. Shelykh, Transport properties of a two-dimensional electron gas dressed by light, *Phys. Rev. B* **91**, 155312 (2015).
- [44] O. V. Kibis, S. Morina, K. Dini, and I. A. Shelykh, Magneto-electronic properties of graphene dressed by a high-frequency field, *Phys. Rev. B* **93**, 115420 (2016).
- [45] I. Crassee, J. Levallois, A. L. Walter, M. Ostler, A. Bostwick, E. Rotenberg, T. Seyller, D. Van Der Marel, and A. B. Kuzmenko, Giant faraday rotation in single- and multilayer graphene, *Nat. Phys.* **7**, 48 (2011).
- [46] M. Shah, N. A. Khan, and M. Sajid, Optical conductivity of ultra thin floquet topological insulators, *J. Phys. D* **55**, 415103 (2022).
- [47] A. A. Burkov and L. Balents, Weyl Semimetal in a Topological Insulator Multilayer, *Phys. Rev. Lett.* **107**, 127205 (2011).
- [48] A. A. Burkov, Topological properties of Dirac and Weyl semimetals, *Reference Module in Materials Science and Materials Engineering* (Elsevier, Amsterdam, 2022).
- [49] M. Shah and M. S. Anwar, Valley and spin polarized quantized spin dependent photonic shifts in topological silicene, *Phys. Lett. A* **401**, 127342 (2021).
- [50] M. Tahir, K. Sabeeh, and U. Schwingenschlögl, Quantum magnetotransport properties of ultrathin topological insulator films, *J. Appl. Phys.* **113**, 043720 (2013).
- [51] N. P. Butch, K. Kirshenbaum, P. Syers, A. B. Sushkov, G. S. Jenkins, H. D. Drew, and J. Paglione, Strong surface scattering in ultrahigh-mobility Bi₂Se₃ topological insulator crystals, *Phys. Rev. B* **81**, 241301(R) (2010).
- [52] L. Wu, W.-K. Tse, M. Brahlek, C. M. Morris, R. V. Aguilar, N. Koirala, S. Oh, and N. P. Armitage, High-Resolution Faraday Rotation and Electron-Phonon Coupling in Surface States of the Bulk-Insulating Topological Insulator Cu_{0.02}Bi₂Se₃, *Phys. Rev. Lett.* **115**, 217602 (2015).
- [53] L. Wu, M. Salehi, N. Koirala, J. Moon, S. Oh, and N. Armitage, Quantized faraday and kerr rotation and axion electrodynamics of a 3d topological insulator, *Science* **354**, 1124 (2016).
- [54] C. Li, B. de Ronde, A. Nikitin, Y. Huang, M. S. Golden, A. de Visser, and A. Brinkman, Interaction between counter-propagating quantum hall edge channels in the 3d topological insulator BiSbTeSe₂, *Phys. Rev. B* **96**, 195427 (2017).
- [55] A. Taskin, H. F. Legg, F. Yang, S. Sasaki, Y. Kanai, K. Matsumoto, A. Rosch, and Y. Ando, Planar hall effect from the surface of topological insulators, *Nat. Commun.* **8**, 1340 (2017).